



RESEARCH

# An involute gear pair meshing stiffness model considering time-varying friction under mixed lubrication

Xin Pei · Jiahong Nie · Haotian Guo · Song Li · Yangjie Zuo

Received: 3 January 2024 / Accepted: 20 July 2024 / Published online: 3 August 2024  
© The Author(s), under exclusive licence to Springer Nature B.V. 2024

**Abstract** To investigate the meshing characteristics of involute spur gear pairs, a time-varying mesh stiffness (TVMS) model is developed in this study, which pays special attention to the nonlinearity of lubrication and friction in the meshing process. Here, to improve the modeling quality, four typical parameters are considered in the model, including the lubrication state, the non-Newtonian shear characteristics of the lubricant, the time-varying displacement of the asperity, and contact conditions along the meshing path. The proposed model provides an interdependence between tooth surface contact characteristics and gear comprehensive meshing stiffness, which can provide a guidance for enhancing the performance of involute spur gears. Furthermore, the effects of roughness, rotation speed, and load on TVMS are investigated, exhibiting distinct regional characteristics along the meshing path. Noticeable

differences are observed in the intensity of disturbance in the meshing-in, meshing-out, single-tooth pair, and double-tooth pair contact areas.

**Keywords** TVMS · Friction · Involute spur gear · Lubrication

## Abbreviations

$d_c$	Distance between the contact point and the tooth root
$h_c$	Distance between contact point and the tooth central line
$E$	Elastic modulus
$F$	Action load
$a$	Semi-axis of the Hertzian contact width
$k_a$	Radial compression stiffness
$k_b$	Bending stiffness
$k_f$	Stiffness considering fillet-foundation deflection
$k_c$	Interface stiffness
$k_s$	Shear stiffness
$k_t$	Overall mesh stiffness
$r$	Reference radius
$r_c$	Distance from gear center to contact point on tooth flank profile
$Z$	Teeth number
$\alpha_c$	Pressure angle
$\beta$	Load angle
$\theta$	Half tooth angle

X. Pei · H. Guo · Y. Zuo (✉)

Key Laboratory of Advanced Spatial Mechanism and Intelligent Spacecraft, Ministry of Education, School of Aeronautics and Astronautics, Sichuan University, Chengdu 610065, China  
e-mail: zuoyangjie@scu.edu.cn

J. Nie

College of Aerospace Engineering, Chongqing University, Chongqing 400044, China

S. Li

Automotive Engineering Research Institute, Byd Auto Industry Company Limited, Shenzhen 518000, China

$u$	Parameter of rack-cutter flank profile equations
$L$	Width of the gear tooth
$u_1, u_2$	Contact center velocity of driving gear and driven gear, respectively
$u_e$	Entraining velocity
$h$	Local film thickness (or gap)
$p$	Pressure
$P_h$	Maximum Hertzian contact pressure
$r_q$	Surface root mean square roughness
$R_{cx}$	Effective radius in the $x$ -direction
$t$	Time
$v_e$	Surface elastic deformation
$s_1, s_2$	Asperity height of Surfaces on driving gear and driven gear, respectively
$\eta, \eta_0$	Viscosity, and viscosity under ambient condition
$\rho_0$	Density under ambient condition
$T_1, T_2$	Local temperature on Surfaces of driving gear and driven gear, respectively
$\mu_1, \mu_2$	Poisson's ratios of driving gear and driven gear, respectively

## 1 Introduction

The lubrication state and friction are pivotal aspects, which affect the transmission efficiency and dynamic characteristics of the gear pair [1]. During the transmission process, the interface contact state constantly changes due to the alternating contact of single and double tooth pairs, the continuous changes in the position of the meshing point, and the load distribution between tooth pairs. Mechanically processed involute gears inevitably have micro-roughness. The movement of the asperity can cause changes in the contact gap and friction, which in turn alter the TVMS characteristics of the gears. This phenomenon is one of the primary sources of dynamic excitation in gear transmission systems [2]. Hence, it is important to study the meshing characteristics of gears.

In recent years, scholars have conducted extensive research on the TVMS of gears. Chaari et al. [3] derived an analytical formula for solving the meshing stiffness by calculating the fillet foundation deflection, based on the widely used Weber formula. Yang et al. [4] proposed an energy method to solve the meshing

stiffness by considering bending, axial compression, and Hertzian contact. Then, Liang et al. [5] simplified the transition curve of the gear and developed an improved energy method to get the TVMS of a planetary gear system. Saxena et al. [6] introduced interface friction into the calculating of gear meshing stiffness, however, the difference in friction direction between the wheel and pinion were not considered. Mao et al. [7] proposed an improved potential energy method based on the slice grouping method to calculate the meshing stiffness of bevel gears with tooth surface topography. Based on fractal roughness, the effects of pressure angle, pitch angle, tooth width and fractal dimension on a bevel gear pair meshing stiffness were studied. In addition, wear [8], assembly errors [9], gear modifications [10], etc. will cause changes in the TVMS of the gear pair. Wang et al. [11] found that planetary gears under mixed lubrication exhibit rich bifurcation characteristics, and tooth surface friction could cause the system to enter chaotic motion in advance. Detailed tribo-dynamic analysis of gear contacts and internal excitation is essential in electric powertrains to improve performance and efficiency.

However, the current calculation method of TVMS has limited consideration of lubrication and friction due to the complexity of roughness contact. Existing studies have rarely taken into account the time-varying films and the movement of asperities. Early researchers attempted to determine the lubrication status of gears by using specific full-film lubrication diagrams that were based on dimensionless elastic and viscosity parameters [12–14]. Mughal et al. [14] pointed out that under high contact pressure, the oil film behaves like an amorphous solid, and an appropriate analytical lubrication models in TVMS models can improve the accuracy of gear dynamic response significantly. Based on smooth elastohydrodynamic lubrication (EHL) model, Zhou et al. [15] found that the amplitude and fluctuation of oil film stiffness are closely related to the shear rate, and the stiffness of the oil film is greater than the interface stiffness of the gear, which has a great impact on gear transmission [16]. Xiao and Shi [17] claimed that under EHL lubrication, crown modification will significantly affect the stiffness and damping of the gear contact point. By rationally designing the gear parameters, it is possible to obtain the appropriate oil film stiffness and damping, which can help reduce the impact and vibration of the gear.

Bobach et al. [18] emphasized that during the gear transmission process, the interaction of surface roughness and film microfluidics plays important roles in stiffness, and their effects cannot be ignored. Using empirical formulas to simplify the consideration of lubrication and friction in the gear meshing process cannot provide insight into the impact of lubricant rheology and contact tribology properties on TVMS changes.

A calculation method for TVMS of involute spur gear pairs is developed in this study, which pays special attention to the nonlinearity of lubrication and friction in the meshing process. Potential energy method [4] is applied to predict the flexibility of gears and gear bodies. The surface pressure is calculated based on a general mixed EHL model [19]. Contact deformation is solved by numerical integration based on elastic half space assumption [20, 21]. The transient friction at the interface is calculated by combining the non-Newtonian viscoelastic lubrication model [27] and the point heat source integration method [24]. The corner contact effect [22] was overlooked in this study. The proposed model focuses on the movement of the actual machined surface during the time-varying meshing process of gears, as well as transient lubrication and friction. Through, corner contact has a significant effect on the shape of the mesh stiffness

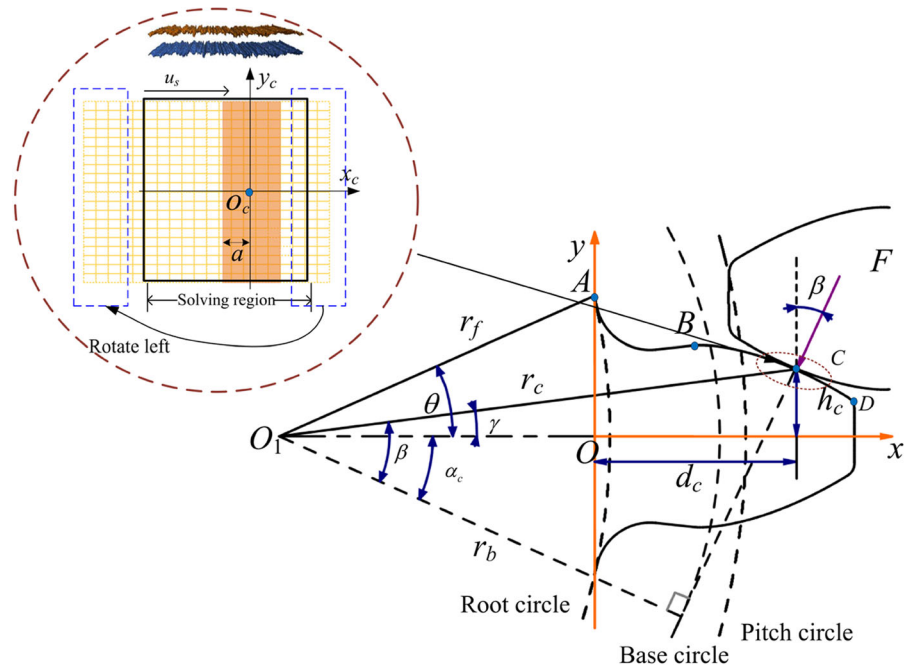
curves [23–25]. By comparing the low-speed smooth solution with the existing literature results based on Hertz, the accuracy of the model was verified, the effects of surface roughness, speed, and load on the TVMS of an involute spur gear pair were analyzed, which can provide valuable guidance for enhancing the performance of involute spur gears.

## 2 Gear mesh modeling

### 2.1 Tooth geometry

Figure 1 shows a variable cross-section beam model of gear meshing forces. There are two coordinate systems in Fig. 1. A Cartesian coordinate system  $S_O(x,y)$  is established by taking the symmetry line of the gear tooth as the  $x$ -axis and the straight line passing through the tangent point (A) of the tooth fillet and the tooth root circle as the  $y$ -axis. Another Cartesian coordinate system  $S_c(x,y)$  takes the tooth surface meshing center as the origin and the tooth surface tangent direction as the  $x$ -axis.  $O_1$  is the rotation center,  $r_b$  is the base circle radius,  $r_f$  is the tooth root circle radius,  $r_c$  represents the distance between the contact point and  $O_1$ ,  $\alpha_c$  is the contact point pressure angle,  $\beta$  is the angle between the contact point and the

**Fig. 1** Beam model of a spur gear tooth



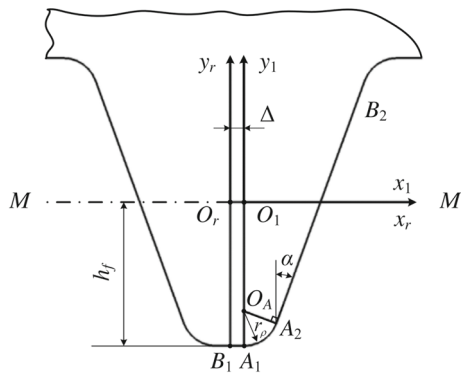


**Fig. 2** Tooth shape of gear cutter and relative coordinate systems [27]

$y$ -axis, and  $\theta$  corresponds to half of the central angle.  $S_c(x,y)$  is the interface contact coordinate system. What transferred from the  $S_O$  coordinate system to  $S_c$  is the tangential velocity of the contact surfaces and the meshing force  $F$ . The transformation of velocity can refer to Eq. (A-1) in Appendix A.

The gear root fillet generated by the tip fillet of the tool can be represented in the coordinate system  $S_o(x, y)$  as [26],

$$\begin{cases} x_{AB} = (-t_p + r\varphi) \sin(\varphi - \theta) + C_1 \cos(\varphi - \theta) - s \\ y_{AB} = (-t_p + r\varphi) \cos(\varphi - \theta) + C_1 \sin(\varphi - \theta) \end{cases} \quad (1)$$

where,  $C_1 = r + r_\rho \sin \alpha - h - \sqrt{r_\rho^2 - t_p^2}$ ,

$$t_p \in [0, r_\rho \cos \alpha],$$

$$s = r_f \cos \theta,$$

$$h = h_f - (1 - \sin \alpha)r_\rho,$$

$$\varphi(t_p) = (r_\rho \sin \alpha - h)t_p / (r\sqrt{r_\rho^2 - t_p^2}),$$

$$\theta = \pi/Z - \Delta/r.$$

$r$  is the reference radius.  $Z$  is the tooth number.  $\Delta$ ,  $r_\rho$ , and  $\alpha$  are tool parameters, which are the distance between the tool tip fillet arc center and the tool symmetry line, tip fillet radius and tooth profile angle of the tool, as shown in Fig. 2.

The involute profile equations in coordinate system  $S_O(x, y)$  can be expressed by [26],

$$\begin{cases} x_{BD} = (-t_p + r\varphi) \sin(\varphi - \theta) + C_2 \cos(\varphi - \theta) - s \\ y_{BD} = (-t_p + r\varphi) \cos(\varphi - \theta) + C_2 \sin(\varphi - \theta) \end{cases} \quad (2)$$

where,  $C_2 = r + \cot \alpha(t_p - \rho \cos \alpha) - h$ ,

$$t_p \in [r_\rho \cos \alpha, (mh_{a^*} + h) \tan \alpha + r_\rho \cos \alpha],$$

$$\varphi(t_p) = [t_p \csc^2 \alpha - (r_\rho \cot \alpha \cdot \cos \alpha + h) \cot \alpha] / r.$$

### 2.2 Tooth and fillet-foundation deflections

The potential energy method has been widely used in solving tooth deflection as well as the TVMS [5, 28]. Tooth deflection consists of bending deflection, shear deflection, and axial compressive deflection. Therefore, there are three types of elastic potential energy associated with the meshing gear tooth: bending, shear, and axial compressive energy. Combining the potential energy method with the tooth profile equation [29], the bending potential energy  $U_b$ , shear potential energy  $U_s$ , and axial compression potential energy  $U_a$  can be expressed as

$$U_b = \int_0^{\rho \cos \alpha} \frac{3[F_b(d_c - x_{AB}(u) - F_a h_c)]^2}{4ELy_{AB}^3(u)} \cdot \frac{dx_{AB}(u)}{du} du + \int_{\rho \cos \alpha}^{u_c} \frac{3[F_b(d_c - x_{BD}(u) - F_a h_c)]^2}{4ELy_{BD}^3(u)} \cdot \frac{dx_{BD}(u)}{du} du \quad (3)$$

$$U_s = \int_0^{\rho \cos \alpha} \frac{1.2F_b^2}{4GLy_{AB}(u)} \cdot \frac{dx_{AB}(u)}{du} du + \int_{\rho \cos \alpha}^{u_c} \frac{1.2F_b^2}{4GLy_{BD}(u)} \cdot \frac{dx_{BD}(u)}{du} du \quad (4)$$

$$U_a = \int_0^{\rho \cos \alpha} \frac{F_a^2}{4ELy_{AB}(u)} \cdot \frac{dx_{AB}(u)}{du} du + \int_{\rho \cos \alpha}^{u_c} \frac{F_a^2}{4ELy_{BD}(u)} \cdot \frac{dx_{BD}(u)}{du} du \quad (5)$$

where,  $\alpha_c = \arccos(r_b/r_c)$ ,

$$\gamma = (\pi + 4e \tan \alpha) / (2Z) + \text{inv} \alpha - \text{inv} \alpha_c,$$

and

$$u_c = (\theta - \gamma)r \sin^2 \alpha + (\rho \cos^2 \alpha + h \sin \alpha) \cos \alpha.$$

$E$  and  $G$  represent elastic and shear moduli, respectively.  $h_c$  is the distance from the gear contact point to tooth central line,  $d_c$  is the distance between the contact point and the tooth root.  $L$  is the tooth width.

The gear meshing process can be divided into two stages: meshing-in and meshing-out. These stages are divided based on the pitch nodes. In the meshing-in stage, the driving gear meshes from the tooth root to the pitch node. At this stage, the speed of the driven gear is greater than that of the driving gear. Thus,  $F_a = F \sin \beta + F_f \cos \beta, F_b = F \cos \beta - F_f \sin \beta$ . In the meshing-out stage, the speed of the driven gear is smaller than that of the driving gear.  $F_a = F \sin \beta - F_f \cos \beta, F_b = F \cos \beta + F_f \sin \beta$ . Detailed calculation methods of friction  $F_f$  are discussed in Sect. 2.3.

By solving for the normal approach height under various loads, the interface contact stiffness can be calculated. The normal contact stiffness can be obtained by using the stress-strain increment relationship.

$$k_c = \left| \frac{F_c^{load1} - F_c^{load2}}{\delta_c^{load1} - \delta_c^{load2}} \right| \tag{6}$$

The interface normal strain  $\delta_c$ , taking into account the fluid load and the actual machined surface, can be determined by solving the Reynolds equation. This topic will be further discussed in Sect. 2.3.

The deformation stiffness of the tooth base is calculated by the formula proposed by Sainsot et al. [30].

$$k_f = \frac{Eb}{\cos^2 \beta \{L \times (u_f/S_f)^2 + M \times (u_f/S_f) + P \times (1 + Q \times \tan^2 \beta)\}} \tag{7}$$

$L, M, P$  and  $Q$  are four coefficients according to the polynomial functions in Sainsot et al. [30]. And they are further explained in Appendix A.

Then, the comprehensive meshing stiffness of the gear can be expressed as:

$$k_t = 1 / (1/k_{b1} + 1/k_{s1} + 1/k_{a1} + 1/k_{b2} + 1/k_{s2} + 1/k_{a2} + 1/k_c) \tag{8}$$

The subscripts 1 and 2 represent the driving gear and the driven gear respectively.

### 2.3 Lubricated contact for spur gear pairs

The time-varying meshing process of the tooth surface is solved in the  $Sc(x,y)$  coordinate system as shown in Fig. 1. During the meshing process of the gear, the interface may have both asperity contact and

hydrodynamic pressure effects, which can be governed by the Reynolds equation.

$$\frac{\partial}{\partial x} \left( \frac{\rho h^3}{12\eta} \frac{\partial p}{\partial x} \right) + \frac{\partial}{\partial y} \left( \frac{\rho h^3}{12\eta} \frac{\partial p}{\partial y} \right) = u_e \frac{\partial(\rho h)}{\partial x} + \frac{\partial(\rho h)}{\partial t} \tag{9}$$

where,  $h$  is the gap between the contact tooth pair, and it can be expressed as a function of geometry, surface roughness, elastic deformation, and offset distance.  $p$  is pressure.  $\eta$  is the viscosity of the lubricant.  $u_e$  is entraining velocity, which is the average of the two tooth surface velocities.

$$h = \delta_c(t) + \frac{x^2}{2R_{cx}} + v_e(x, y, t) + s_1(x, y, t) + s_2(x, y, t) \tag{10}$$

In Eq. (10),  $R_{cx}$  is the equivalent radius in the  $x$  directions, whose calculation method is shown in Appendix A,  $v_e$  represents the elastic deformation,  $s_1$  and  $s_2$  are the two surface asperity height.  $\delta_c$  is the interface normal strain or normal approach height.

Elastic deformation can be convolved by the following formula:

$$v_e(x, y, t) = \frac{2}{\pi E'} \iint_{\Omega} \frac{p(\xi, \varsigma)}{\sqrt{(x - \xi)^2 + (y - \varsigma)^2}} d\xi d\varsigma \tag{11}$$

where  $E'$  represent the equivalent elastic modulus. Its calculation method can refer to Appendix A.

The viscosity is calculated by the equation proposed by Roelands.[31]

$$\eta = \eta_0 \exp \left[ (\ln \eta_0 + 9.67) (1 + 5.1 \times 10^{-9} p)^{0.68} - 1 \right] \tag{12}$$

The unit of  $p$  in the above equation is Pa. The unit of  $\eta_0$  is Pa·s. The density can be obtained from the following formula, where  $\rho_0$  is the density at normal pressure.

$$\frac{\rho}{\rho_0} = 1 + \frac{0.6 \times 10^{-9} p \times m^2/N}{1 + 1.7 \times 10^{-9} p \times m^2/N} \tag{13}$$

The normal approach height  $\delta_c$  is adjusted through the load balance equation:

$$F_c(t) = \iint_{\Omega} p(x, y, t) dx dy \tag{14}$$

If the calculated resultant force is less than  $F_c$ , then  $\delta_c$  needs to be reduced, Otherwise, add  $\delta_c$ , so that the equation holds. By obtaining  $\delta_c^{load1}$  and  $\delta_c^{load2}$  under two adjacent loads ( $F_c^{load1}$  and  $F_c^{load2}$ ), the meshing stiffness of the interface can be obtained through Eq. (6).

Friction causes the temperature to rise and reduces the viscosity of the fluid, the reduction in viscosity will reduce friction to a certain extent. Friction and temperature affect each other, so they need to be solved simultaneously. The contact state of each discrete point in the solution area can be determined according to the value of film thickness  $h$ . In the boundary lubrication contact region ( $h = 0$ ), a fixed friction coefficient 0.14 is used. Boundary friction coefficient is often in a range of 0.07–0.15 for lubrication systems with commonly used steels and industrial lubricants [32]. In the EHL contact region ( $h > 0$ ), the EHL friction is calculated by the method proposed by Bair–Winer[33].

$$\begin{cases} \dot{\gamma} = \frac{\dot{\tau}}{G_\infty} - \frac{\tau_L}{\eta} \ln\left(1 - \frac{\tau}{\tau_L}\right) \\ G_\infty(p, T) = \frac{1.2p}{2.52 + 0.024T} - 10^8 \cdot \\ \tau_L(p, T) = 0.25G_\infty \end{cases} \quad (15)$$

$\dot{\gamma}$  is shear rate.  $\tau$  and  $\dot{\tau}$  are the shear stress and the derivative of shear stress with time, respectively. The unite of  $p$  is Pa.

It is assumed that the heat generated by the contact is completely taken away by the gear, and the convection of the lubricant and the normal heat flow can be ignored. These simplifications have been proven feasible and widely adopted[34]. The temperature can be calculated iteratively by the following equation [35, 36]:

$$\begin{cases} T_1(\xi) = T_{b1} + \left(\frac{1}{\pi\rho_1 C_1 u_1 k_1}\right)^{0.5} \int_{-x}^{\xi} \left\{ \frac{k_{ff}}{h} [T_2(\lambda) - T_1(\lambda)] + \frac{q(\lambda)}{2} \right\} \times \frac{d(\lambda)}{(\xi - \lambda)^{0.5}} \\ T_2(\xi) = T_{b2} + \left(\frac{1}{\pi\rho_2 C_2 u_2 k_2}\right)^{0.5} \int_{-x}^{\xi} \left\{ \frac{k_{ff}}{h} [T_1(\lambda) - T_2(\lambda)] + \frac{q(\lambda)}{2} \right\} \times \frac{d(\lambda)}{(\xi - \lambda)^{0.5}} \end{cases} \quad (16)$$

where  $q$  is the shear heat.  $T_{b1}$  and  $T_{b2}$  are volume temperature of the gear pair, and  $k_{ff}$  is the thermal conductivity of the lubricant.  $C_1$  and  $C_2$  are specific heat.  $k_1$  and  $k_2$  are thermal conductivity of the gear pair.  $\lambda$  is the one-dimensional conduction coordinates.

$u_1$  and  $u_2$  represent the velocities of the two surfaces, respectively.

It should be pointed out that in the solution of lubrication, the kinematics of gears are considered rather than dynamics. By solving the geometric and motion parameters of gears along the meshing path, the transient lubrication and friction characteristics under the meshing path are studied.

### 2.4 Overall deformation of tooth pair and load distribution

The overall deformation of meshing tooth pairs consists of contact deformation ( $\delta_c$ ), bending deformation ( $\delta_b$ ), shear deformation ( $\delta_s$ ), axial compression deformation ( $\delta_a$ ), and the deformation of gear matrix ( $\delta_f$ ). The subscripts 1 and 2 represent the driving gear and the driven gear respectively.

$$\begin{aligned} \delta = \delta_c + \delta_{b1} + \delta_{s1} + \delta_{a1} + \delta_{f1} + \delta_{b2} + \delta_{s2} + \delta_{a2} \\ + \delta_{f2} \end{aligned} \quad (17)$$

The load distribution between the gear pairs that mesh instantaneously can be approximately represented as:

$$F_i = \frac{k_i}{\sum_j^n k_j} F = \frac{F_i}{\delta_i} \times \frac{F}{\sum_j^n \frac{F_j}{\delta_j}} \quad (18)$$

where,  $F_i$  represents the meshing force on the  $i$ -th tooth,  $\delta_i$  is the total deformation of the  $i$ -th tooth contact.  $k_i$  is the meshing stiffness of the  $i$ -th tooth,  $n$  is the number of teeth participating in the instantaneous meshing. The flow chart of the calculation process is shown in Fig. 3.

The calculation of mixed EHL approach is shown in Fig. 4. First, the meshing path is discretized, and the surface topography, comprehensive curvature radius, surface speed, load, etc. of each contact position on the discrete path are obtained. Then, the contact conditions at each location are substituted into the Reynolds equation. The Reynolds equation is solved by the finite difference method, initial values of pressure and normal approach height are based on Hertzian contact, and they are corrected through relaxation iteration method. After the results converge, the friction and temperature rise of the interface are calculated. Three-

**Fig. 3** Flow chart of the computational procedure to obtain meshing force

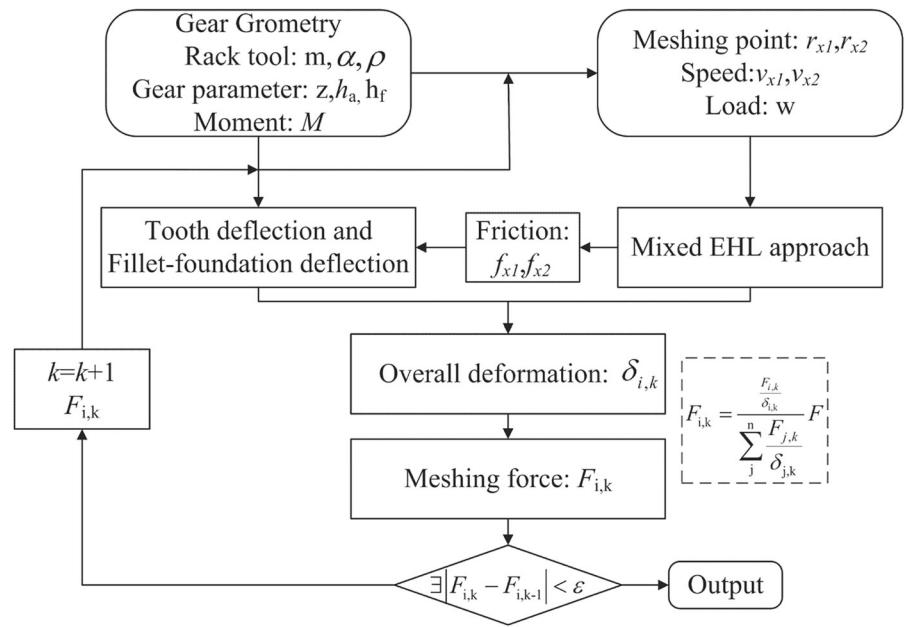
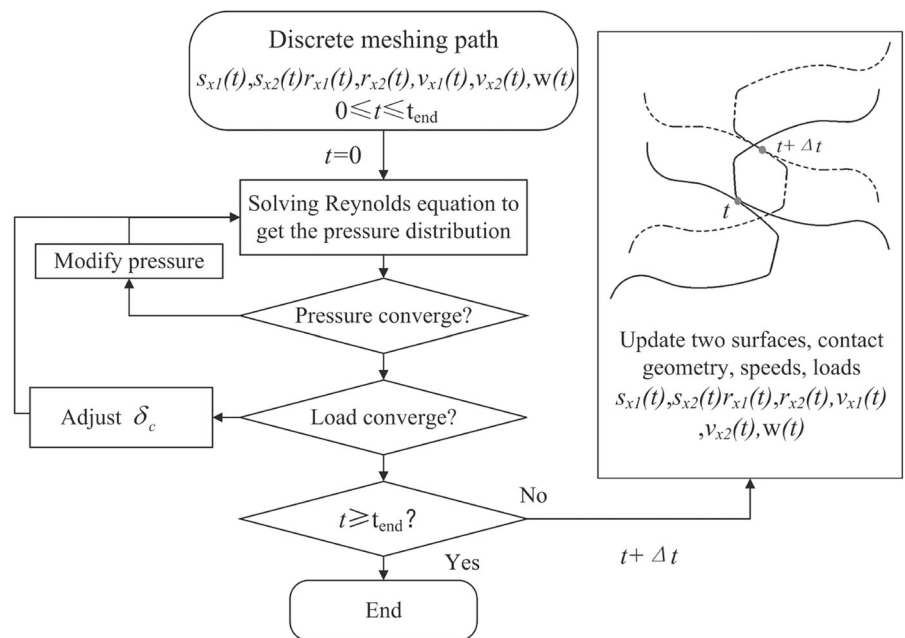


**Fig. 4** Flow chart of the computational procedure to obtain friction and interface normal strain



dimensional infinite line contact is used in the simulation, that is, multiple grids are divided in the y direction, while the edge effects in the y direction are ignored. This is to avoid the strong randomness of the rough peaks in a two-dimensional model. To capture the movement and updates of the surface during the

meshing process, three layers of meshes are utilized, consisting of two rough surface meshes and a solution area mesh. The two surface meshes are denser than the mesh in the region where the Reynolds equation is solved. The two surface meshes do not directly participate in the iteration of the Reynolds equation,

**Table 1** Details of gear parameters

Parameters	Pinion/Wheel
Teeth number	36
Module (mm)	4
Width (mm)	12
Pressure angle (°)	20
Addendum coefficient	1.0
Tip clearance coefficient	0.25
Elastic modulus (GPa)	206.8
Poisson's ratio	0.3

but interact with the solution region through mapping. After the solution at time  $t$  is completed, the grid of the solution area is updated based on the distance moved. To minimize computing costs, the grid of the rough surface only needs to be wider than the contact area. Through continuous queue movement, the desired movement effect can be achieved.

The solution area is divided into  $256 \times 100$  grids, with  $-4 a_0$  to  $2.8 a_0$  in  $x$  direction, and  $-L/2$  to  $L/2$  in  $y$  direction.  $a_0$  is the Hertzian contact width at the meshing-in position.  $L$  is the width of gear tooth.

The relaxation iteration coefficient for pressure is 0.005, and the basis for convergence is as follows.

$$\begin{cases} \sum |p_{ij}^{new} - p_{ij}^{old}| / \sum p_{ij}^{old} \leq 0.000001 \\ \left| \iint_{\Omega} p_{x,y} dx dy - F_c \right| \leq 0.0001 \end{cases} \quad (19)$$

### 2.5 Basic simulation parameters

Two identical involute spur gears are used in the simulation, and the detailed parameters are shown in Table 1. Three-dimensional scanning of the machining topography, as shown in Fig. 5, is adapted in the numeral calculations of interface contact characteristics, and the normal misalignment of the initial contact position is used to avoid possible nesting of the surfaces. The surface consists of  $2937 \times 1881$  nodes. The initial viscosity of the lubricant is 0.023 Pa·s at room temperature (24 °C) and standard atmospheric pressure. The gear meshing path is discretized into 3000 points to ensure smooth convergence of mixed EHL approach. By adjusting the height of the

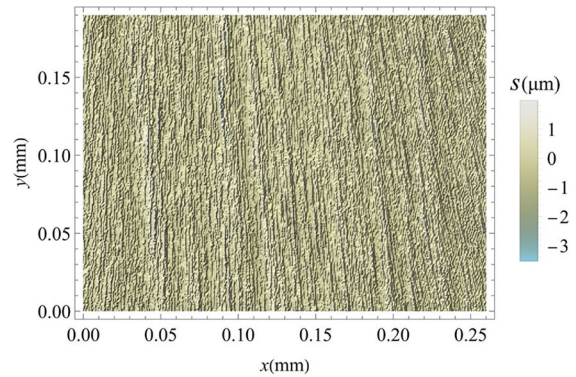


**Fig. 5** Three-dimensional scanning of the machining topography

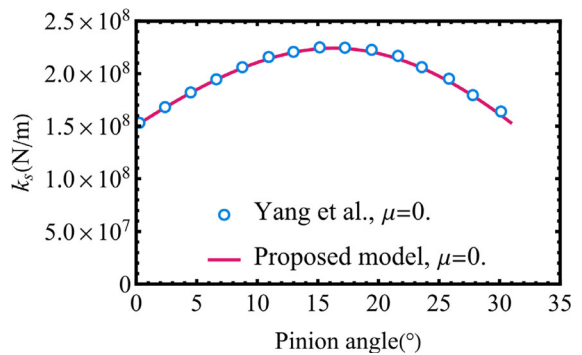


**Fig. 6** Comparison between single tooth pair mesh stiffness evolutions yielded by Yang et al. [27] and the proposed model

asperities, the roughness of simulated surface can be scaled to the desired value.

### 2.6 Model verification

It should be pointed out that the model is based on kinematics of gears and kinetics/dynamics is neglected; hence, the stiffness model validation is conducted at very low speed and can be representative since dynamics effects are not included in the simulations. When the gear speed is very low, the contacts experience boundary lubrication. At this time, the hydrodynamic pressure effect of the lubricant ceases, and the interface transitions into a Hertzian contact state. Therefore, the simulation results of the smooth surface at an extremely low speed of 1 rpm can be compared with those based on the Hertzian contact to verify the accuracy of the proposed model.



Figure 6 shows a comparison of the elasticity and mixed EHL results at extremely low speeds. The simulation results of the mixed EHL approach at extremely low speeds show good consistent with the model of Yang et al.[27], which is based on Hertz theory. This is in line with the expectation that the lubricating film disappears and only Hertz contact remains at extremely low speeds. The gear parameters used for verification are shown in Appendix A-Table 2. The consistency between the extremely low-speed and Hertz solutions confirms the correctness of the proposed model at extremely low speeds.

### 3 Results and discussions

#### 3.1 Surface roughness

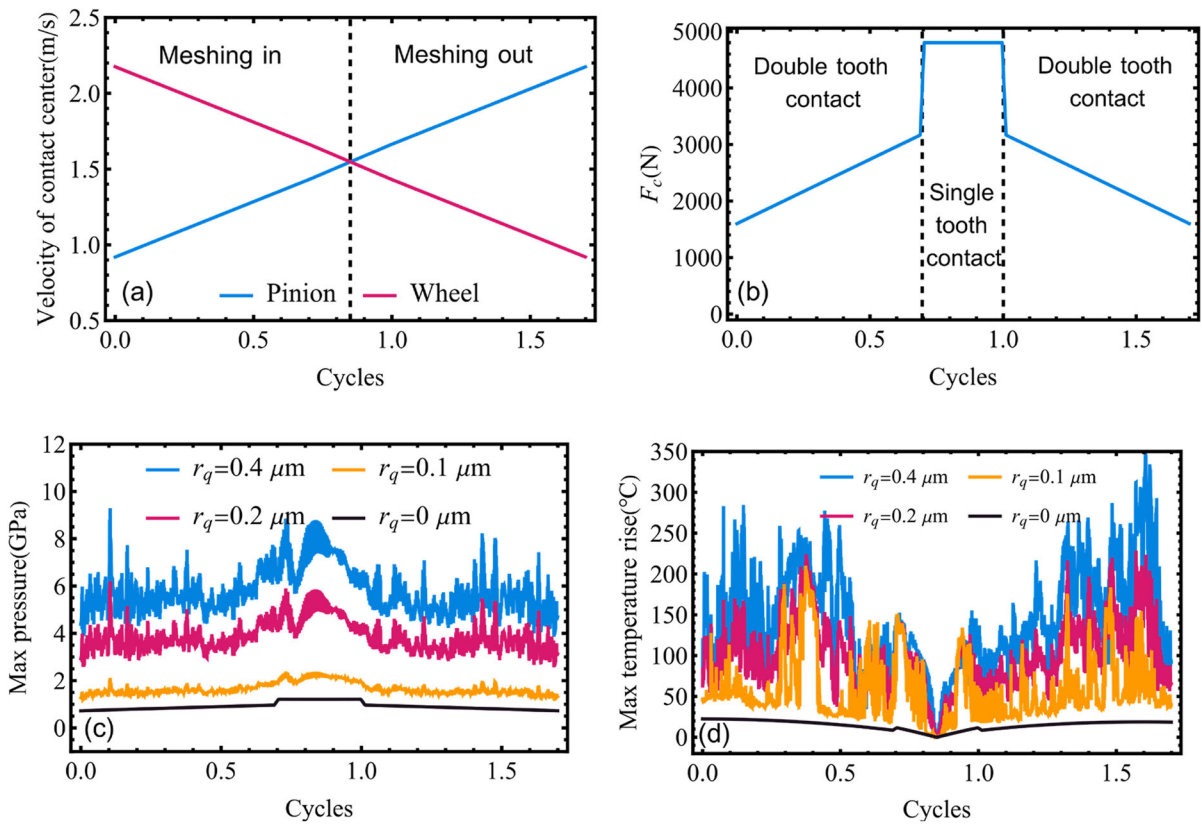
Surface roughness has a significant impact on contacts. A rough surface can increase the friction between gears and decrease the efficiency of mechanical components. Due to variations in machining accuracies, the roughness of gears is typically falls within the micrometer range, which is usually comparable to the film thickness of tooth pair contacts during operation. In this section, the analysis focuses on the effects of roughness on contact characteristics and gear meshing stiffness, the torque is 345.6 Nm, and the input rotation speed is 600 rpm.

Figure 7 shows the variation in velocity, load, maximum surface pressure and maximum surface temperature rise during a mesh cycle. It can be seen that for smooth surfaces, the maximum pressure change is consistent with the change in contact point load, but for rough surfaces, there is no obvious correlation between the maximum surface pressure and the contact load. This is because that for the rough cases, the maximum pressure source is mainly the elastic deformation of the local asperity, which is highly random. In addition, for the smooth cases, the maximum surface temperature rise is obviously affected by the relative sliding speed and the load distribution along the meshing path. As the relative sliding speed decreases during the meshing stage, the maximum surface temperature rise decreases. Where the teeth mesh alternately (at 0.69 and 1.0 cycle), there is a sudden change in surface temperature rise.

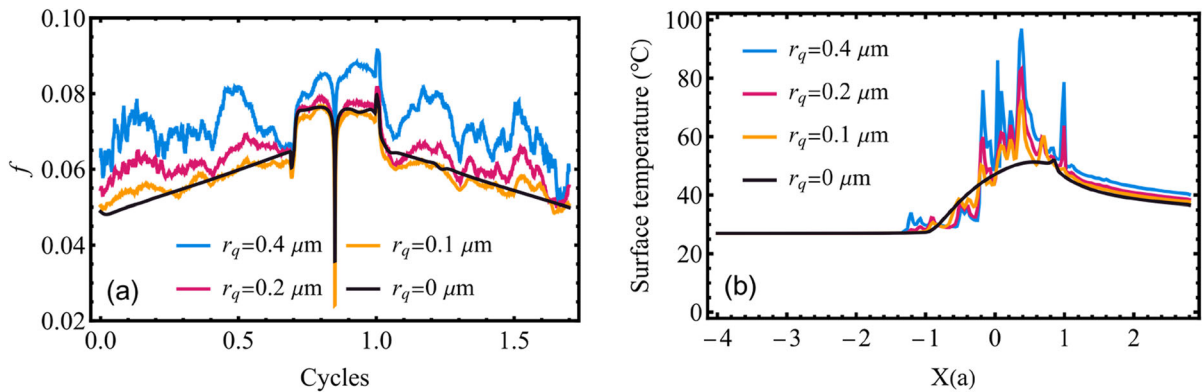
However, this pattern is also not significant when considering roughness. An obvious temperature rise reduction is only observed when the relative sliding speed is low (at 0.85 cycle).

Figure 8a illustrates the changes in the friction coefficient along the meshing path under four different roughness conditions. It is evident that the roughness has a significant impact on friction. As the roughness of tooth surface increases, the fluctuation of the friction coefficient along the meshing path also increases. For smooth contact, the friction coefficient along the meshing path is also not fixed. At the alternating meshing of single and double tooth pairs, the friction coefficient experiences two sudden changes due to transient impact. When the roughness is relatively large, the sudden changes are not very significant because the friction coefficient fluctuates along the meshing path. For example, the change in friction coefficient of  $r_q = 0.4 \mu\text{m}$  at the alternating meshing of single and double tooth pairs is relatively insignificant compared to the other three cases. At the gear pitch circle, the slip-roll ratio is 0, and theoretically, the fluid friction at this point is also 0. However, the friction coefficient here in the fig is reduced to a minimum value instead of being 0. This is because the path is discretized, and the discretized contact points always have small relative sliding velocities, as well as possible partial asperity contact. Figure 8b demonstrates the temperature rise at the meshing-in position. It can be observed that the surface temperature rise is significantly affected by the roughness peak distribution, and there are random peaks that are particularly strong. The surface temperature rise, taking into account roughness, is significantly greater than that of a smooth surface. Additionally, the maximum temperature rise increases as the roughness increases.

Figure 9 demonstrates the film thickness and pressure distribution at the meshing-in position. Under the smooth surface, the oil completely separates the two surfaces, creating an evenly distributed film gap between the two tooth surfaces. However, due to the roughness, the contact occurs in mixed lubrication, and some of the asperities come into direct contact. The greater the roughness, the higher the pressure peak, increasing the likelihood of film breakage and intensifying direct contact between asperities. When the roughness moves, the distribution of gaps and



**Fig. 7** variation of contact characters during a mesh cycle **a** Velocity, **b** Load, **c** Max pressure, **d** Max temperature rise of pinion



**Fig. 8** Friction and temperature of gear contacts under different roughness. **a** Evolution of friction coefficient along the meshing path, **b** Temperature Distribution on the plane  $Y = 0$  at the meshing-in position

pressure at the interface changes. If the effect of roughness is ignored, the resulting interface contact characteristics may be too idealized.

Data in Fig. 10a suggests that roughness affects the normal approach height of the tooth pair interface. As roughness increases, the height of normal contact also

increases. This may be because the rougher the surface, the higher the peaks of asperity. The higher the asperity peak at the same normal approach height, the greater the strain and pressure generated. In addition, while the normal approach height fluctuates slightly, it is not as significant as the change in the

transient friction coefficient. The normal approach height initially decreases almost linearly during the double-tooth meshing-in stage, then remains almost constant during the single-tooth pair contact stage, and finally increases linearly during the meshing-out stage.

As shown in Fig. 10b, the interface stiffness increases significantly in the double-tooth pair meshing-in stage, remains relatively constant in the single-tooth pair contact area, and decreases significantly during the double-tooth meshing-out stage. At the alternating

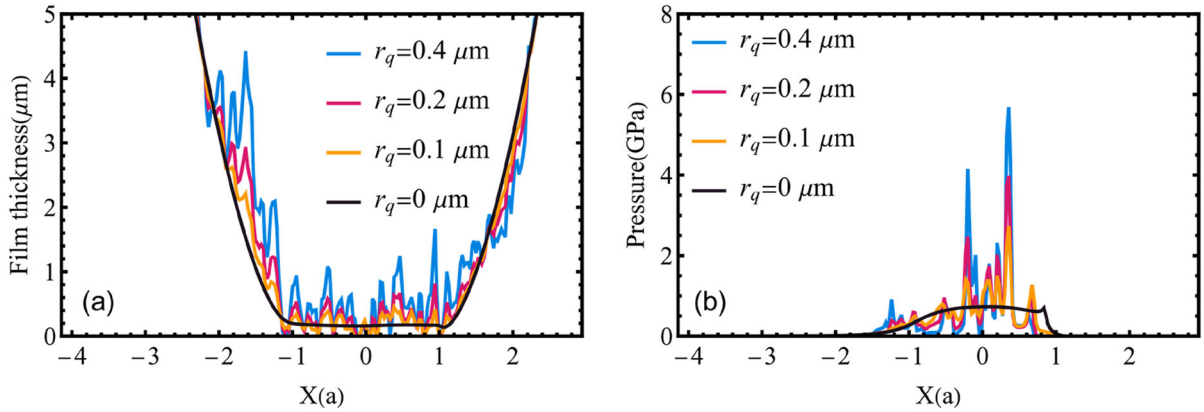


**Fig. 9** Contact properties on the plane  $Y = 0$  at the meshing-in position. **a** Film thickness distribution, **b** Pressure distribution

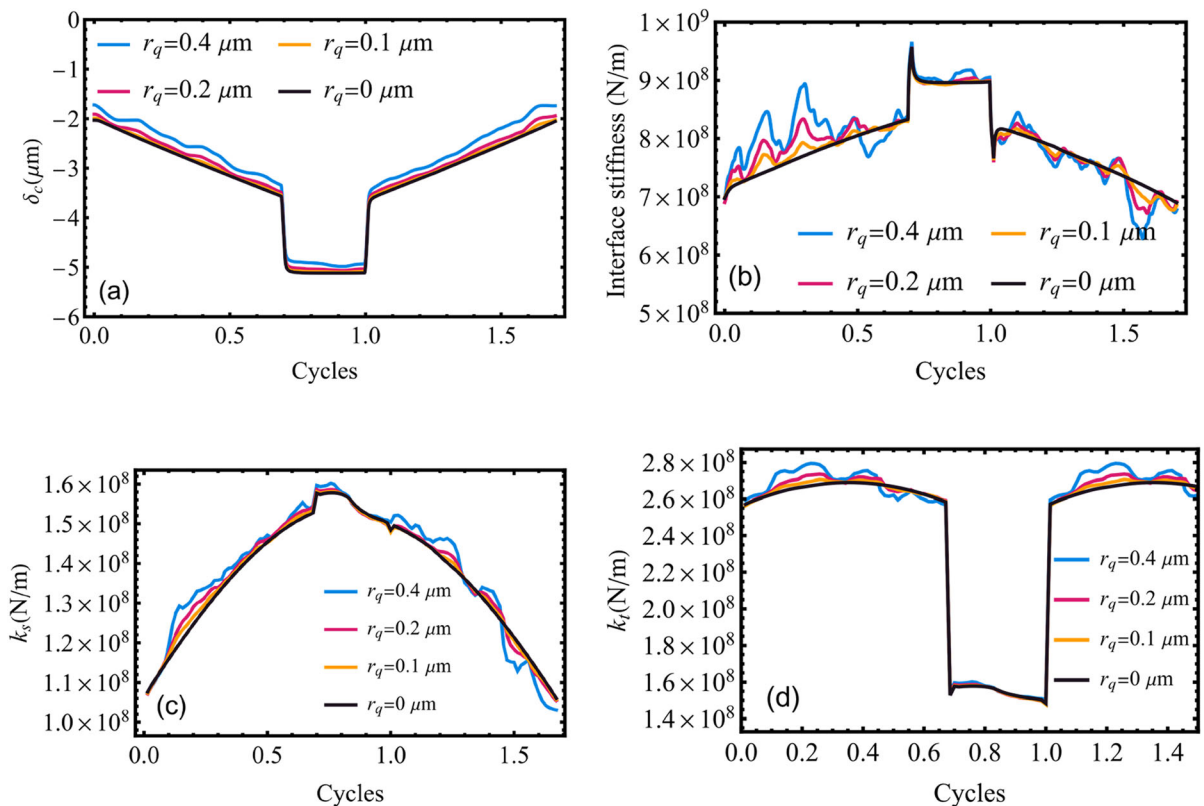


**Fig. 10** Evolutions of normal approach height and gear mesh stiffness for different roughness. **a** Normal approach height, **b** Interface stiffness, **c** Mesh stiffness of a single tooth, **d** Comprehensive mesh stiffness of gears

meshing of single and double tooth pairs, the interface stiffness experiences transient peaks and valleys as a result of transient changes in load. It should be pointed out that in actual engineering, this fluctuation may not be so severe due to the corner contact, which may be a shortcoming of this model. Roughness has a significant impact on the stiffness of the interface, particularly in the area where the double-tooth pairs meshing occurs. The fluctuation of interface stiffness increases with the increase of roughness. Comparing the single-tooth and comprehensive meshing stiffness in Fig. 10c-d, it can be observed that roughness has a greater impact on the stiffness of the multi-tooth pair meshing area.

### 3.2 Velocity

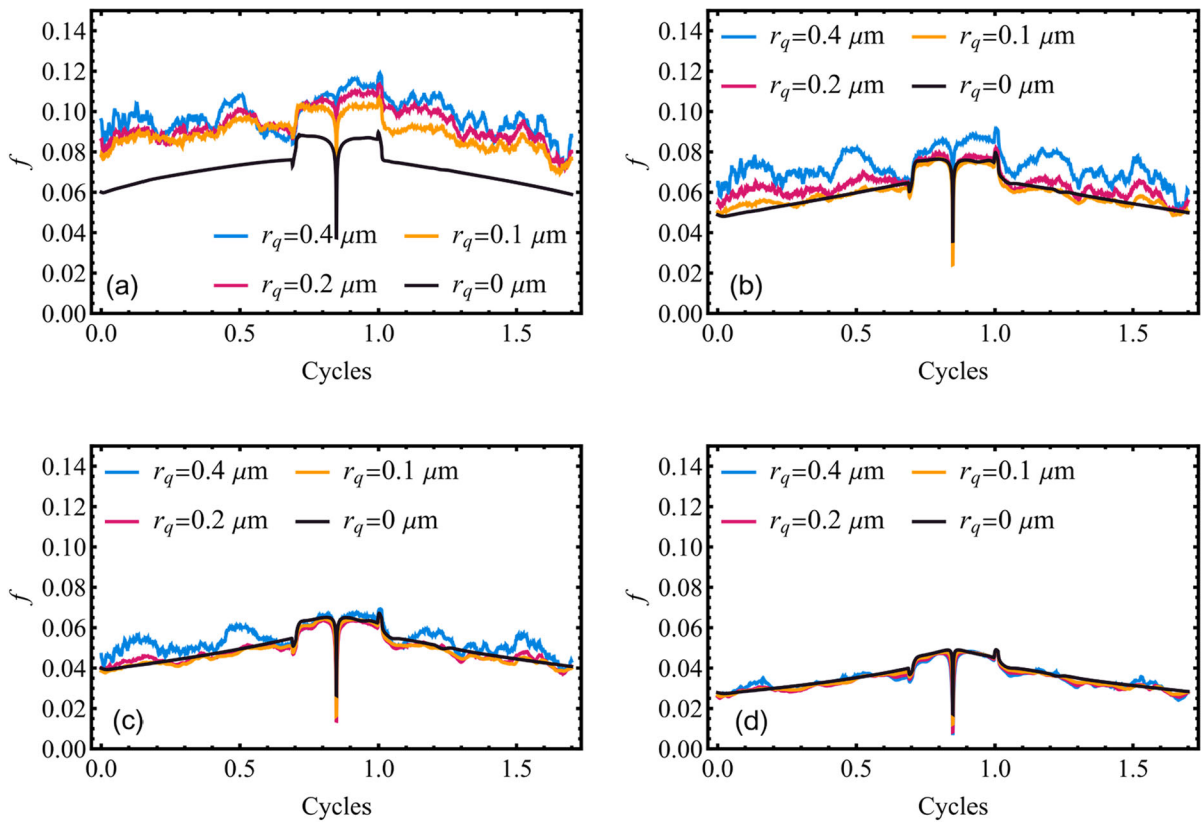
Velocity has a great influence on the lubrication state of gear contacts. Ideally, the lubricant can completely isolate the two tooth surfaces at the appropriate entraining velocity. Lubricant serves as a spring that connects the interface of gear tooth pairs, providing a buffering effect during the meshing process. It is commonly known that, within a certain range, as the speed increases, the film thickness will increase, and the friction will decrease. The changes in oil film thickness and friction may impact the stiffness of the interface and the comprehensive meshing stiffness of gear pair. Therefore, this section compares the interface friction and stiffness characteristics at various input speeds, while the torque is 345.6 Nm. Figure 11a-d demonstrate the evolution of friction coefficient along the meshing path at four speeds respectively.

At low speeds and on smooth surfaces, even with a small entrainment speed, the elastohydrodynamic effect is still significant. This results in the formation of a stable oil film, leading to a low friction coefficient. Rough surfaces make it easier to break the oil film. It can be seen from Fig. 11a that when the input speed is 60 rpm, the friction coefficient based on the smooth surface is significantly lower than that of the rough surfaces. However, the difference in friction coefficient under different roughness surfaces at 6000 rpm is small. At high speeds, although the friction coefficient fluctuates locally due to the influence of roughness, there is not a significant difference in the overall friction coefficient between a smooth surface and a rough surface, as shown in Fig. 11d. However, as the

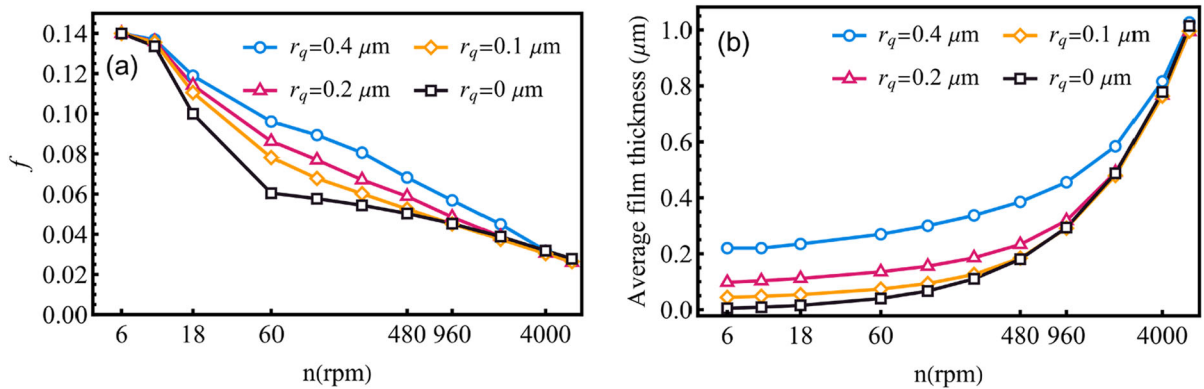
speed decreases, the impact of roughness on the friction coefficient becomes more pronounced.

Figure 12 shows the variation of the Interface characteristics at the meshing-in position with input speed under four different roughness conditions. At both extremely low speed and high speeds, the curves of different roughness essentially overlap. This is because that there is only solid friction at extremely low speeds. Since there are peaks and valleys on the rough surface, the average oil film thickness is not 0 even at low speeds. This phenomenon is caused by the fact that there is always lubricant in the valleys of the rough surface. The film load-bearing capacity is reduced at extremely low speed and more asperity contacts may occur. While, at high speeds, lubricants can bear more load, the lubrication conditions are favorable. The shear force of the lubricant is minimal, and a stable film reduces the impact of rough peaks on lubrication. In most of the speed range in Fig. 12, such as 18–2000 rpm, although the friction coefficient decreases with the increase in speed under different roughness, their values are obviously different. The greater the roughness at the same speed, the larger the friction coefficient, which is consistent with engineering experience.

Figure 13 shows the simulation results at different speeds when the roughness is 0.2  $\mu\text{m}$ . As can be seen from Fig. 13a, the influence of speed on normal approach height is obvious. The greater the speed, the thicker the oil film, resulting in the farther the distance between the two surfaces. At different speeds, there is obvious stratification in the normal approach height, while the difference in tangential stiffness of the interface is not significant. Figure 13b shows that the tangential stiffness of the interface fluctuates to a certain extent along the meshing path, and the fluctuation decreases as the speed increases. Comparing Fig. 13c and d, it can be found that speed has an impact on gear meshing stiffness. For a single tooth pair, in the meshing-in stage, the single-tooth meshing stiffness at low speed is large, while in the meshing-out stage, the meshing stiffness at high speed is large. Gear meshing is an alternating meshing of single and double gear tooth pairs. Due to the comprehensive effect of double tooth pairs meshing, in the double teeth meshing area, the comprehensive stiffness does not differ much. In the single tooth pair meshing area, there are certain differences in the overall meshing stiffness at different speeds. The overall meshing



**Fig. 11** Evolution of friction coefficient along meshing path at different rotation speeds for different roughness. **a** 60 rpm, **b** 600 rpm, **c** 1800 rpm, **d** 6000 rpm



**Fig. 12** Interface characteristics versus rotation speeds at the meshing-in position. **a** Friction coefficient; **b** Average film thickness

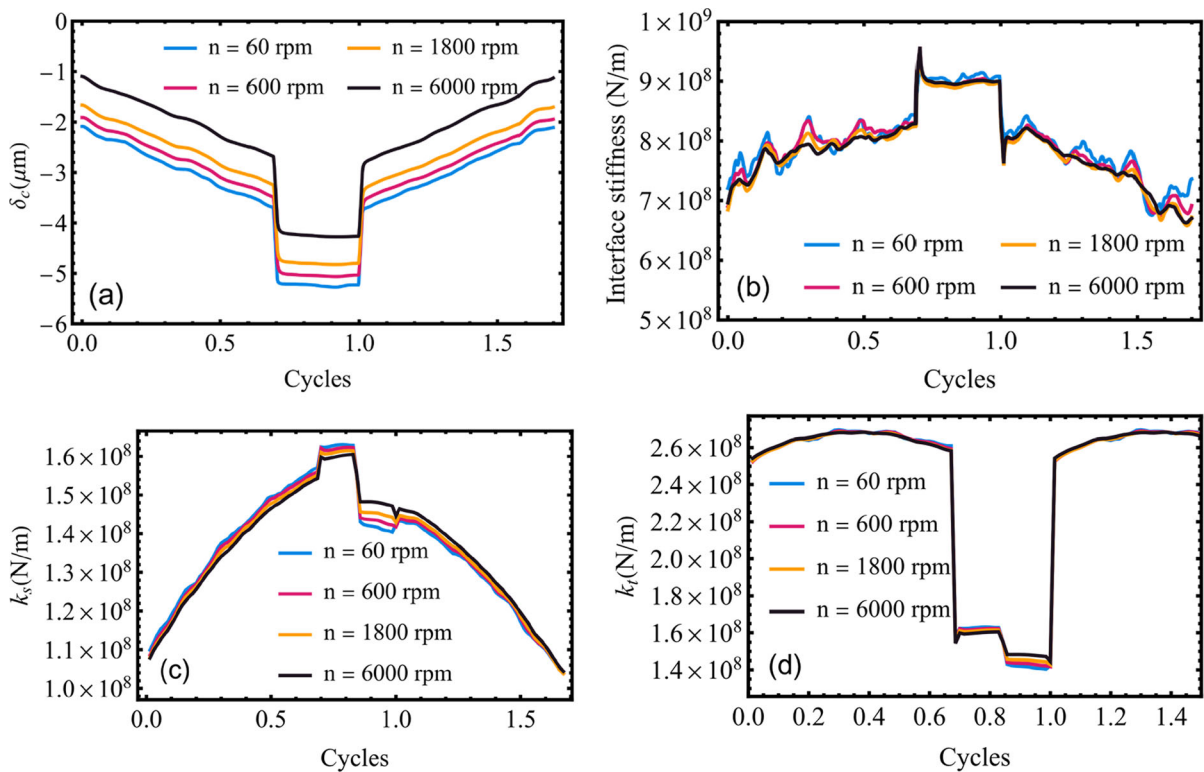


**Fig. 13** Evolutions of normal approach height and gear mesh stiffness for different speeds. **a** normal approach height, **b** Interface stiffness, **c** Mesh stiffness of a single tooth, **d** Comprehensive mesh stiffness of gears

stiffness in the single tooth pair meshing area changes larger at low speeds.

### 3.3 Load

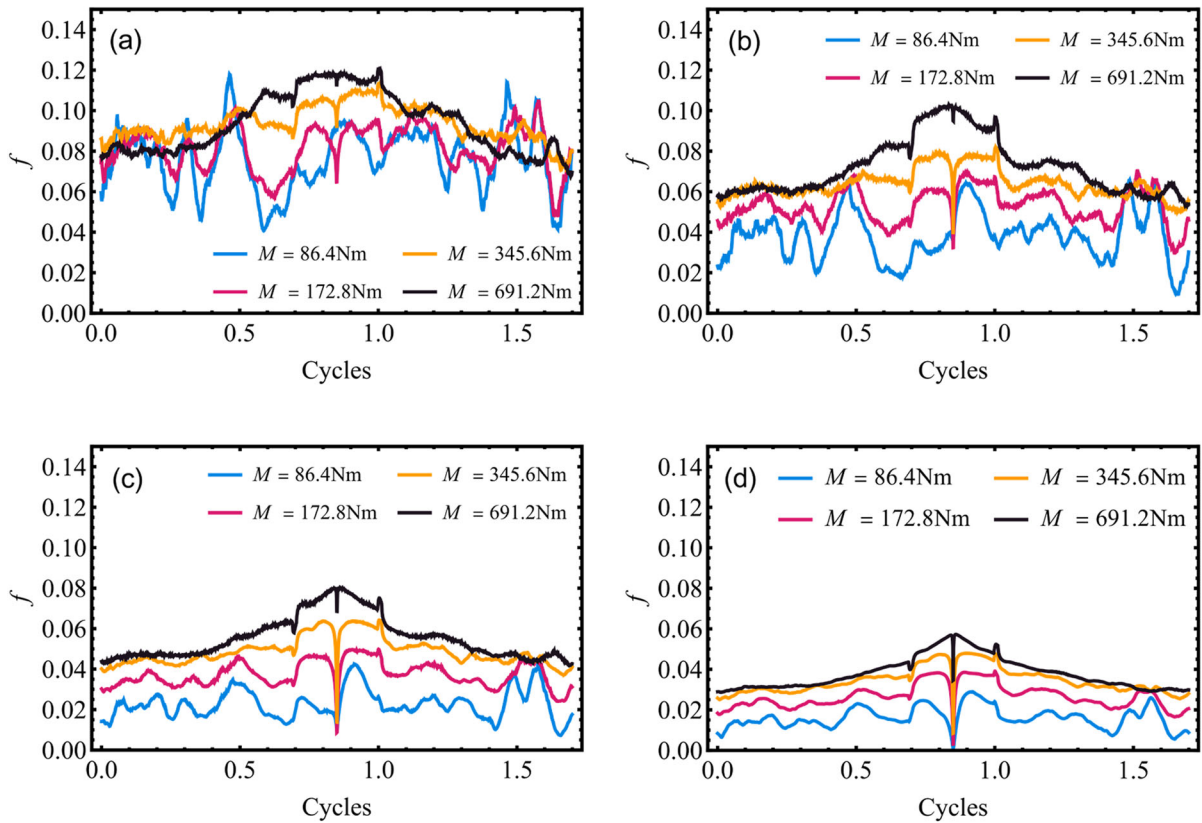
Generally, as the load increases, the film becomes thinner, the normal approach height decreases, and the actual load-bearing area increases. These changes may have an impact on the friction of the interface and the stiffness of the gear mesh. So, this section discusses the effect of load on gear interface friction and stiffness.

Figure 14 illustrates the evolution of the tooth surface friction coefficient along the meshing path under different torques. The surface roughness used in the cases is  $0.2 \mu\text{m}$ . Under different input speeds, the change in friction coefficient becomes smoother as the load increases. The friction coefficient is the largest under heavy load ( $M = 691.2\text{N}\cdot\text{m}$ ). This may be because the deformation area is larger under heavy load, making it easier for the asperities to be flattened and resulting in a smoother change in the friction

coefficient. Therefore, appropriately increasing the load on the tooth surface can enhance the stability of gear meshing.

Based on the working conditions of the meshing-in position, the relationship between load and tooth surface friction is further discussed. Data in Fig. 15 suggests that there is a positive correlation between load and the friction coefficient. As the load increases, the friction coefficient tends to increase, but this trend gradually weakens.

It can be seen from Fig. 16a that, as the load increases, the normal approach height decreases, and there is significant variation in the normal approach height under different loads. The difference between the normal approach height under a torque of  $86.4\text{Nm}$  and that under a torque of  $691.2\text{Nm}$  is approximately  $10 \mu\text{m}$ . Although the normal approach heights under different loads vary greatly, the differences in interface tangential stiffness are not particularly significant. Figure 16b shows that the fluctuation of interface stiffness along the meshing path is larger under light load compared to heavy load. For the



**Fig. 14** Evolution of friction coefficient along meshing path at different rotation speeds for different loads. **a** 60 rpm **b** 600 rpm **c** 1800 rpm **d** 6000 rpm

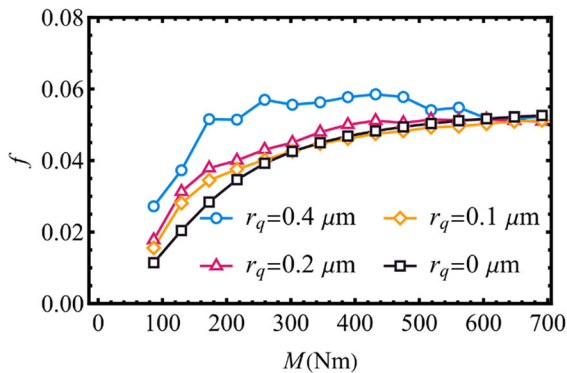


**Fig. 15** Friction coefficient vs. torque at the meshing-in position

meshing stiffness of a single tooth pair in Fig. 16c, in the meshing area of a single tooth pair, the change in meshing stiffness is smaller under light load compared to heavy load, primarily due to the low friction coefficient. Figure 16d demonstrates that the

fluctuation of comprehensive meshing stiffness is large in the multi-tooth pairs meshing area under light load, while the fluctuation in the single-tooth pair meshing area is small. Conversely, under heavy load, the pattern is opposite.

#### 4 Conclusions

A TVMS model was developed in this study for involute spur gear pairs. The model considers the nonlinear friction caused by the movement of asperities and the time-varying conditions of meshing, as well as the time-varying stiffness of the mixed lubrication interface. This allows for a more accurate prediction of the overall meshing stiffness of gear pairs. The effects of surface roughness, rotating speed, and gear moment on friction and stiffness are analyzed and discussed. The results show that:

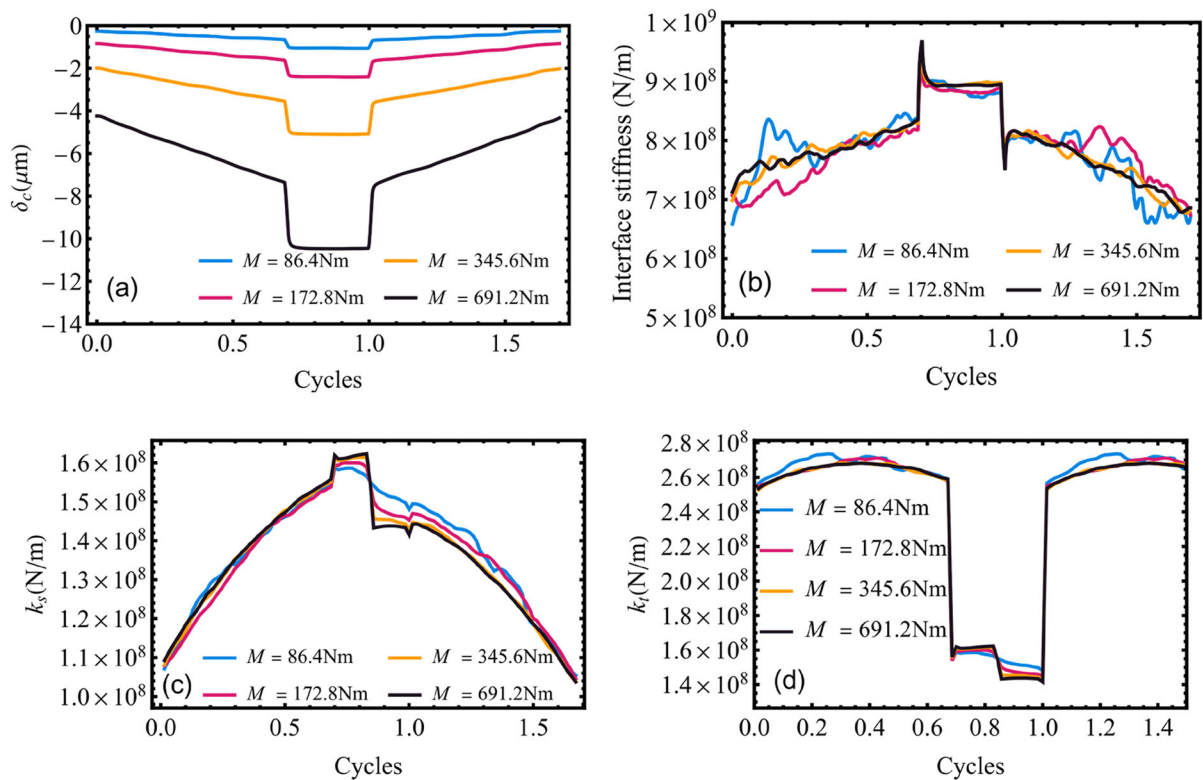


**Fig. 16** Evolutions of normal approach height and gear mesh stiffness for different loads. **a** normal approach height, **b** Interface stiffness, **c** Mesh stiffness of a single tooth, **d** Comprehensive mesh stiffness of gears

- (1) The increase in tooth surface roughness will not only increase interface friction and frictional force fluctuation, but also lead to an increase in gear meshing stiffness fluctuation, particularly in the area where multiple tooth pairs are meshing.
- (2) The movement of asperities will have an impact on friction and meshing stiffness across a wide speed range. At high rotational speeds, the EHL film helps to reduce the disturbances caused by roughness.
- (3) Increasing the load can reduce the fluctuation of friction on the tooth surface, but it will also increase the friction force and stiffness fluctuation in the meshing area of a single tooth pair. Under light loads, the deformation area of the tooth surface is small, the meshing stiffness in

the double tooth pair meshing area experiences significant fluctuations.

## 5 The deficiencies of the model

It should be pointed out that the traditional meshing force calculation model, which does not consider the influence of corner contact, is used in our study. When the corner contact effect is taken into account, the load evolution along the meshing path will be more natural, which can reduce the sudden change in stiffness at the alternation of single and double teeth pair meshing. This is the deficiencies of the present model.

See Tables 2, 3.



**Table 2** Coefficients of polynomial in Eq. (A-2)

	$A_i$	$B_i$	$C_i$	$D_i$	$E_i$	$F_i$
$L$	$- 5.574 \times 10^{-5}$	$- 1.9986 \times 10^{-3}$	$- 2.3015 \times 10^{-4}$	$4.7702 \times 10^{-3}$	0.0271	6.8045
$M$	$6.0111 \times 10^{-4}$	$2.81 \times 10^{-2}$	$- 8.3431 \times 10^{-3}$	$- 9.9256 \times 10^{-3}$	0.1624	0.9086
$P$	$- 5.0952 \times 10^{-4}$	0.1855	$0.538 \times 10^{-5}$	$5.33 \times 10^{-2}$	0.2895	0.9236
$Q$	$- 6.2042 \times 10^{-5}$	$9.0889 \times 10^{-3}$	$- 4.0964 \times 10^{-4}$	$7.8297 \times 10^{-3}$	$- 0.1472$	0.6904

**Table 3** Parameters of the gear for comparison with Yang et al. [27]

Parameters	Pinion	Wheel
Teeth number	19	48
Module (mm)	4	4
Width (mm)	16	16
Pressure angle (°)	20	20
Addendum coefficient	1.0	1.0
Tip clearance coefficient	0.25	0.25
Elastic modulus (GPa)	206.8	206.8
Poisson’s ratio	0.3	0.3

**Acknowledgements** The study has been supported by the National Natural Science Foundation of China (NSFC, No. 52305067), Natural Science Foundation of Sichuan (No. 2023NSFSC0869), and the Opening Project of Key Laboratory of Advanced Spatial Mechanism and Intelligent Spacecraft, Ministry of Education (Sichuan University).

**Author contribution** Xin Pei: Methodology, Software, Writing – original draft. Jiahong Nie: Software, Review, Suggestion. Haotian Guo: Methodology, Suggestion, review. Song Li: Software, Review, Suggestion. Yangjie Zuo: Methodology, Suggestion, Writing – review & editing.

**Funding** The funding was provided by National Natural Science Foundation of China, 52305067, Natural Science Foundation of Sichuan, 2023NSFSC0869, Opening Project of Key Laboratory of Advanced Spatial Mechanism and Intelligent Spacecraft, Ministry of Education (Sichuan University).

**Data availability** No datasets were generated or analysed during the current study.

**Declarations**

**Conflict of interest** The authors declare no competing interests.

**Appendix A**

The following are the transformation of velocity from the  $S_O$  coordinate system to  $S_c$ .

$$\begin{cases} g_{yc} = \mp \frac{1}{2} d_1 \text{Sin} \alpha \pm \sqrt{\left(\frac{1}{2} d_1 \text{Sin} \alpha\right)^2 - \left(\frac{1}{2} d_1\right)^2 + r_c^2} \\ r_1 = \frac{1}{2} d_1 \text{Sin} \alpha \pm \\ r_2 = \frac{1}{2} d_1 \text{Sin} \alpha \mp g_{yc} \\ u_{1,2} = \omega_{1,2} \times r_{1,2} \end{cases} \tag{A - 1}$$

The subscripts 1 and 2 represent the driving gear and the driven gear.  $d_1$  is the pitch circle diameter of the driving gear.  $\alpha$  is the pressure angle.  $r$  is the contact curvature radius of the two gears.  $u$  denotes velocity speed at the contact point.  $\omega$  is the angular velocity.

The following are intermediate variables defined in Eqs. (7),

$$X^*(h_f, \theta_f) = \frac{A_i}{\theta_f^2} + B_i h_f^2 + \frac{C_i h_f}{\theta_f} + \frac{D_i}{\theta_f} + E_i h_f + F_i \tag{A - 2}$$

$X^*$  indicates the coefficients  $L$ ,  $M$ ,  $P$  and  $Q$ . The values of  $A_i$ ,  $B_i$ ,  $C_i$ ,  $D_i$ ,  $E_i$ , and  $F_i$  are listed in A-Table 1.

The following are the parameters of the gear for comparison with Yang et al.

The formula for calculating the comprehensive curvature radius.

$$\frac{1}{R_{cx}} = \frac{1}{R_1} + \frac{1}{R_2} \tag{A - 3}$$

The formula for calculating the comprehensive elastic modulus.

$$\frac{1}{E'} = \frac{1}{2} \left( \frac{1 - \nu_1^2}{E_1} + \frac{1 - \nu_2^2}{E_2} \right) \quad (\text{A} - 4)$$

## References

- Mughal, H., Dolatabadi, N., Rahmani, R.: An integrated tribodynamic model for investigation of efficiency, durability and NVH attributes of gear mesh in electric vehicle powertrains. *Tribol. Int.* **189**, 108977 (2023)
- Meng, Z., Shi, G., Wang, F.: Vibration response and fault characteristics analysis of gear based on time-varying mesh stiffness. *Mech. Mach. Theory* **148**, 103786 (2020)
- Chaari, F., Fakhfakh, T., Haddar, M.: Analytical modelling of spur gear tooth crack and influence on gearmesh stiffness. *Eur. J. Mech.-A/Solids* **28**, 461–468 (2009)
- Yang D, Lin J. Hertzian damping, tooth friction and bending elasticity in gear impact dynamics. 1987.
- Liang, X., Zuo, M.J., Pandey, M.: Analytically evaluating the influence of crack on the mesh stiffness of a planetary gear set. *Mech. Mach. Theory* **76**, 20–38 (2014)
- Saxena, A., Parey, A., Chouksey, M.: Effect of shaft misalignment and friction force on time varying mesh stiffness of spur gear pair. *Eng. Fail. Anal.* **49**, 79–91 (2015)
- Mao, H., Sun, Y., Xu, T., Yu, G.: Numerical calculation method of meshing stiffness for the beveloid gear considering the effect of surface topography. *Math. Probl. Eng.* **2021**, 1–17 (2021)
- Geng, Z., Xiao, K., Li, J., Wang, J.: Bifurcation and chaos of a spur gear transmission system with non-uniform wear. *J. Vib. Acoust.* **143**, 031004 (2021)
- Liu, C., Shi, W., Liu, K.: Calculation method of mesh stiffness for helical gear pair with manufacturing errors, assembly errors and tooth modifications. *Meccanica* **57**, 541–565 (2022)
- Yang, Y., Wang, J., Zhu, G., Yang, W., Zhou, Q.: A thermomechanical model for mesh deflection calculation of crown spur gear pair. *Meccanica* **55**, 1393–1411 (2020)
- Wang, J., Liu, N., Wang, H., Guo, L.: Research on bifurcation and chaos characteristics of planet gear transmission system with mixed elastohydrodynamic lubrication (EHL) friction. *Int. J. Nonlinear Sci. Num. Simul.* **23**, 1–14 (2022)
- Greenwood, J.: Presentation of elastohydrodynamic film-thickness results. *J. Mech. Eng. Sci.* **11**, 128–132 (1969)
- Schmid SR, Hamrock BJ, Jacobson BO. *Fundamentals of machine elements*: CRC Press; 2013.
- Hamrock, B.J., Dowson, D.: Isothermal elastohydrodynamic lubrication of point contacts: Part 1—Theoretical formulation. *J. Tribol.* **98**, 223–228 (1976)
- Zhou, C., Xiao, Z., Chen, S., Han, X.: Normal and tangential oil film stiffness of modified spur gear with non-Newtonian elastohydrodynamic lubrication. *Tribol. Int.* **109**, 319–327 (2017)
- Xiao, Z., Zhou, C., Chen, S., Li, Z.: Effects of oil film stiffness and damping on spur gear dynamics. *Nonlinear Dyn.* **96**, 145–159 (2019)
- Xiao, Z., Shi, X.: Investigation on stiffness and damping of transient non-Newtonian thermal elastohydrodynamic point contact for crowned herringbone gears. *Tribol. Int.* **137**, 102–112 (2019)
- Bobach, L., Beilicke, R., Bartel, D., Deters, L.: Thermal elastohydrodynamic simulation of involute spur gears incorporating mixed friction. *Tribol. Int.* **48**, 191–206 (2012)
- Ren N, Zhu D, Chen WW, Liu Y, Wang QJ. A Three-Dimensional Deterministic Model for Rough Surface Line-Contact EHL Problems. *Journal of Tribology*. 2008;131.
- Liu, S., Guo, H., Zhou, Q.: Numerical point contact model of mixed elastohydrodynamic lubrication for transversely isotropic coating. *J. Tribol.* **146**, 044101–044111 (2024)
- Pei, X., Yang, W.: Investigation of the misalignment and modification for crown roller contacts under mixed lubrication. *Proc. Inst. Mech. Eng. Part J: J. Eng. Tribol.* **237**, 2098–2111 (2023)
- Parker, R., Vijayakar, S., Imajo, T.: Non-linear dynamic response of a spur gear pair: modelling and experimental comparisons. *J. Sound Vib.* **237**, 435–455 (2000)
- Sakaridis, E., Kalligeros, C., Papalexis, C., Kostopoulos, G., Spitas, V.: Symmetry preserving neural network models for spur gear static transmission error curves. *Mech. Mach. Theory* **187**, 105369 (2023)
- Cirelli, M., Valentini, P.P., Pennestrì, E.: A study of the non-linear dynamic response of spur gear using a multibody contact based model with flexible teeth. *J. Sound Vib.* **445**, 148–167 (2019)
- Yu, W., Mechefske, C.K.: Analytical modeling of spur gear corner contact effects. *Mech. Mach. Theory* **96**, 146–164 (2016)
- Yang, Y., Wang, J., Huang, Y., Yang, W., Zhou, Q.: Stress analysis of coated spur and helical gears considering load distribution. *Proc. Inst. Mech. Eng., Part J: J. Eng. Tribol.* **234**, 649–667 (2020)
- Yang, Y., Wang, J., Zhou, Q., Huang, Y., Zhu, J., Yang, W.: Mesh stiffness modeling considering actual tooth profile geometry for a spur gear pair. *Mech. Industry* **19**, 306 (2018)
- Chen, Z., Shao, Y.: Dynamic simulation of spur gear with tooth root crack propagating along tooth width and crack depth. *Eng. Fail. Anal.* **18**, 2149–2164 (2011)
- Tian X, Zuo MJ, Fyfe KR. Analysis of the vibration response of a gearbox with gear tooth faults. *ASME international mechanical engineering congress and exposition2004*. p. 785–93.
- Sainsot And, P., Velez, P., Duverger, O.: Contribution of gear body to tooth deflections—a new bidimensional analytical formula. *J. Mech. Des.* **126**(4), 748–752 (2004)
- Roelands CJA, Winer WO, Wright W. Correlational aspects of the viscosity-temperature-pressure relationship of lubricating oils (Dr In dissertation at Technical University of Delft, 1966). 1971.
- Ai X. Numerical analyses of elastohydrodynamically lubricated line and point contacts with rough surfaces by using semi-system and multigrid methods.(Volumes I and II). 1995.
- Bair S, Winer WO. A rheological model for elastohydrodynamic contacts based on primary laboratory data. *ASME Journal of Lubrication Technology*. 1979:258–65.

34. Zhu D, Hu YZ. A computer program package for the prediction of EHL and mixed lubrication characteristics, friction, subsurface stresses and flash temperatures based on measured 3-D surface roughness. *Tribology Transactions*. 2001:44.
35. Carslaw HS, Jaeger JC. *Conduction of heat in solids*. Oxford: Clarendon Press, 1959, 2nd ed. 1959.
36. Liu, Y.-C., Wang, H., Wang, W.-Z., Hu, Y.-Z., Zhu, D.: Methods comparison in computation of temperature rise on frictional interfaces. *Tribol. Int.* **35**, 549–560 (2002)

**Publisher's Note** Springer Nature remains neutral with regard to jurisdictional claims in published maps and institutional affiliations.

Springer Nature or its licensor (e.g. a society or other partner) holds exclusive rights to this article under a publishing agreement with the author(s) or other rightsholder(s); author self-archiving of the accepted manuscript version of this article is solely governed by the terms of such publishing agreement and applicable law.